J|A|C|S
ARTICLES

Published on Web 11/24/2010

Origin of the Magnetic Bistability in Molecule-Based Magnets: A First-Principles Bottom-Up Study of the TTTA Crystal

Caroline S. Clarke, Joaquim Jornet-Somoza, Fernando Mota, Juan J. Novoa,* and Mercè Deumal*

Departament de Química Física & IQTCUB, Facultat de Química, Universitat de Barcelona, Martí i Franquès 1, Barcelona, Spain E-08028

Received June 30, 2010; E-mail: juan.novoa@ub.edu; merce.deumal@ub.edu

Abstract: The magnetic bistability present in some molecule-based magnets is investigated theoretically at the microscopic level using the purely organic system TTTA (1,3,5-trithia-2,4,6-triazapentalenyl). The TTTA crystal is selected for being one of the best-studied molecule-based systems presenting magnetic bistability. The magnetic properties of the high- and low-temperature structures (HT and LT phases, respectively) are accurately characterized by performing a First-Principles Bottom-Up study of each phase. The changes that the magnetic exchange coupling constants (J_{AB}) undergo when the temperature is raised (LT → HT) or lowered (HT → LT) are also fully explored in order to unravel the reasons behind the presence of these two different pathways. The triclinic LT phase is diamagnetic due to the fact that the nearly eclipsed π dimer is effectively magnetically silent and not to formation of a covalent bond between two TTTA molecules. It is also shown that bistability in TTTA results from the coexistence of the monoclinic HT and triclinic LT phases in the temperature range studied.

Introduction

Bistability is the ability of a material to present two stable phases that can both exist within a given range of temperatures but above and below that range only one or the other phase exists. Bistability is a key potential property for the development of new devices, notably in data storage, and light or heat sensors.[1] Despite this fact, there is no quantitative description of the microscopic mechanism responsible for this behavior. Thus, a rational design of materials presenting this property and in particular of bistable molecule-based magnets, which are our target, is not yet fully attainable.

An excellent example of experimentally well-characterized bistable molecule-based magnetic materials,[2,3] and thus a prototype of these materials, is provided by crystals of the neutral radical 1,3,5-trithia-2,4,6-triazapentalenyl (TTTA, Figure 1). The TTTA crystal is an organic system presenting magnetic interactions that is bistable at room temperature:[3,4] on heating above 320 K only the 'high-temperature' (HT) paramagnetic phase (monoclinic $P2_1/c$) is observed, and on cooling below 210 K only the 'low-temperature' (LT) diamagnetic phase is present (triclinic $P\bar{1}$) (Figure 2). The only spin-carrying units in these two crystal systems are the doublet TTTA radicals. The radical electron is formally ascribed to the deprotonated N atom in the five-membered dithiazolyl ring (Figure 1a). However, UB3LYP/Aug-cc-pVTZ and UHF/Aug-cc-pVTZ calculations indicate that the unpaired electron is partly delocalized over both heterocyclic rings (Figures 1b and 1c and Table 1), which is confirmed by EPR studies on dilute solutions.[3,7,8] This spin delocalization, also found for similar thiazyls in other calculations[3,5,8,9] and polarized neutron diffraction experiments,[9] allows the presence of multiple magnetic exchange pathways within the crystal. TTTA radicals also show polarization in the electron distribution (Figure 1d) since N atoms hold a net negative charge and S atoms a net positive charge. As a result, a strong dipole moment (0.7929 D) is generated, which has an important influence on the way these radicals arrange when forming crystals.

The crystal packing in the HT paramagnetic phase (monoclinic $P2_1/c$) and the LT diamagnetic phase (triclinic $P\bar{1}$) is similar (see Figure 3), comprising 2D layers that stack in the third dimension. In both crystal structures, two consecutive rows within the same layer (Figures 3a and 3b) are aligned in opposite directions (top row, S leads right; bottom row, S leads left) and present numerous lateral S···N contacts that are shorter than the sum of the S and N van der Waals radii (S···N = 3.20−3.63 Å). Neighboring 2D layers pile up one on top of the other with a $\pi-\pi$ approach of molecules (Figures 3c and 3d). In the HT structure, the stacking of these 2D layers is regular, where all

(1) Kahn, O. *Chem. Br.* **1999**, *35*, 24.
(2) Barclay, T. M.; Cordes, A. W.; George, N. A.; Haddon, R. C.; Itkis, M. E.; Mashuta, M. S.; Oakley, R. T.; Patenaude, G. W.; Reed, R. W.; Richardson, J. F.; Zhang, H. *J. Am. Chem. Soc.* **1998**, *120*, 352.
(3) McManus, G. D.; Rawson, J. M.; Feeder, N.; van Dujin, J.; McInnes, E. J. L.; Novoa, J. J.; Burriel, R.; Palacio, F.; Oliete, P. *J. Mater. Chem.* **2001**, *11*, 1992.
(4) Fujita, W.; Awaga, K. *Science* **1999**, *286*, 261.
(5) Fujita, W.; Awaga, K.; Matsuzaki, H.; Okamoto, H. *Phys. Rev. B* **2002**, *65*, 064434.
(6) CCDC: (a) Allen, F. H. *Acta Crystallogr.* **2002**, *B58*, 380. (b) Allen, F. H.; Motherwell, W. D. S. *Acta Crystallogr.* **2002**, *B58*, 407.
(7) Wolmershauser, G.; Johann, R. *Angew. Chem., Int. Ed. Engl.* **1989**, *28*, 920.
(8) Chung, Y.-L.; Sandall, J. P. B.; Sutcliffe, L. H.; Joly, H.; Preston, K. F.; Johann, R.; Wolmershauser, G. *Magn. Reson. Chem.* **1991**, *29*, 625.
(9) Campo, J.; Luzón, J.; Palacio, F.; Rawson, J. M. In *Carbon-Based Magnetism*; Makarova, T., Palacio., F., Eds.; Elsevier: New York, 2006; Chapter 7.

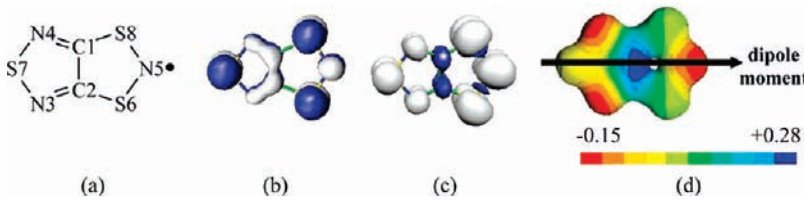

Figure 1. (a) Molecular structure of TTTA (atomic numbering according to spin densities given in Table 1). (b) SOMO of TTTA radical. (c) Spin density (cutoff at 0.0015 au) and (d) molecular electrostatic potential (MEP) map of TTTA where red (blue) indicates regions of negative (positive) electron density (minimum −0.15259 au; maximum +0.28326 au). See representation of the dipole moment of TTTA (0.7929 D). Notice that b and c show π symmetry. Computational level is UB3LYP/6-31+G(d) using the Gaussian03 package.

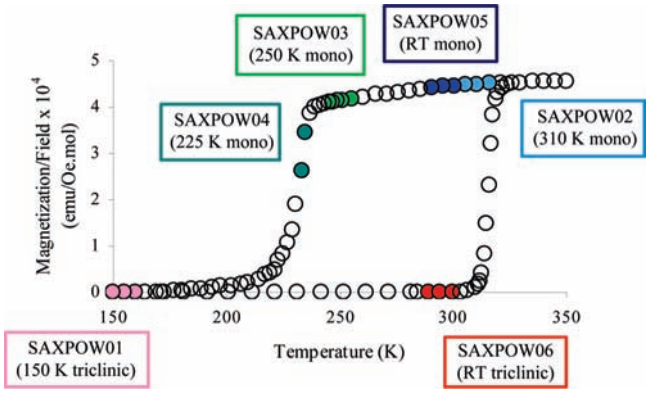

Figure 2. Magnetization plot showing the thermal hysteresis present in the range 210−320 K, where HT and LT structures can both exist. The approximate positions on the hysteresis loop of each of the six published X-ray data sets of the TTTA crystal are also given, of which two correspond to the triclinic phase (recorded at 150 K and room temperature, SAXPOW01 and 06) and four to the monoclinic phase (abbreviated as 'mono' in this figure, recorded at 225 K, 250 K, RT, and 310 K, SAXPOW04, -03, -05 and -02).[3−5] Refcodes SAXPOW01-06 given by the Cambridge Crystallographic Data Base CCDC.[6]

radicals in one stack are separated from their neighbor by the same centroid···centroid distance (3.711 Å in Figure 3c). In the LT structure, the stacking gives rise to dimers of TTTA radicals whose centroids are 3.409 Å apart, which are then separated by a longer 3.784 Å interdimer distance (Figure 3d). This is the main geometrical difference between the HT and the LT structures. Thus, the change in the magnetic properties of the HT and LT structures (from paramagnetic to diamagnetic) has been associated with intrastack spin-paired dimerization.[10] However, this explanation clearly does not take into account the interstack magnetic interactions, whose relevance and strength has not been yet evaluated in detail. Furthermore, the microscopic mechanism by which temperature induces this dimerization is not clear nor why the pathways for the LT → HT and HT → LT transformations should be different.

The bistable region that lies in the 210−320 K range is bounded by a thermal hysteresis loop, and the HT → LT conversion pathway is different from the LT → HT pathway. In the TTTA case, the hysteresis loop encompasses room temperature and thus either phase can be isolated at room temperature using external stimuli, such as light or pressure.[4,5,11] The origins of the bistable region are explored in this work. Six crystallographic structures (SAXPOW01−06 in Figure 2) have been recorded in and around this hysteresis loop at various temperatures, providing a data set that forms the basis of the study performed here. Therefore, in order to obtain a proper understanding of the key factors that determine the mechanism of the hysteretic transformation in TTTA crystals, we performed a study using first-principles methods. The mechanism of the magnetic interaction in the HT and LT phases of the TTTA crystals was investigated using the First-Principles Bottom-Up procedure,[12,13] so as to accurately determine which radical−radical interactions change in the LT → HT and HT → LT phase transformations. It is worth pointing out here that this procedure was recently used successfully to describe the variation of bulk magnetic properties with temperature on a similar dithiadiazolyl radical.[14] Besides basic interest in obtaining a better understanding of the bistability mechanism in dithiazolyls (e.g., TTTA),[2,15] the results presented here can also be of interest in terms of understanding the existence of bistability in other purely organic magnets such as dithiadiazolyls.[16]

Methodological Details

As already mentioned, the study performed in this work is aimed at accurately understanding how the radical···radical magnetic interactions change when going between the LT and the HT structures.

The First-Principles Bottom-Up procedure[12] is used to accomplish this objective. This is a four-step procedure that involves computing the macroscopic magnetic properties, using the experimental crystal structure as the only input. No assumptions of any kind are made concerning the sign or size

(10) Rawson, J. M.; Alberola, A.; Whalley, A. *J. Mater. Chem.* **2006**, *16*, 2560.
(11) Matsuzaki, H.; Fujita, W.; Awaga, K.; Okamoto, H. *Phys. Rev. Lett.* **2003**, *91*, 017403.
(12) Deumal, M.; Bearpark, M. J.; Novoa, J. J.; Robb, M. A. *J. Phys. Chem. A* **2002**, *106*, 1299.
(13) Deumal, M.; LeRoux, S.; Rawson, J. M.; Robb, M. A.; Novoa, J. J. *Polyhedron* **2007**, *26*, 1949.
(14) Deumal, M.; Rawson, J. M.; Goeta, A. E.; Howard, J. A. K.; Copley, R. C. B.; Robb, M. A.; Novoa, J. J. *Chem.—Eur. J.* **2010**, *16*, 2741.
(15) DTAs: (a) Barclay, T. M.; Cordes, A. W.; de Laat, R. H.; Goddard, J. D.; Haddon, R. C.; Meter, D. Y.; Mawhinney, R. C.; Oakley, R. T.; Palstra, T. T. M.; Patenaude, G. W.; Reed, R. W.; Westwood, N. P. C. *J. Am. Chem. Soc.* **1997**, *119*, 2633. (b) Alberola, A.; Collis, R. J.; Humphrey, S. M.; Less, R. J.; Rawson, J. M. *Inorg. Chem.* **2006**, *45*, 1903. (c) Wolmershauser, G.; Schnauber, M.; Wilhelm, T. *J. Chem. Soc., Chem. Commun.* **1984**, 573. (d) Fujita, W.; Awaga, K.; Nakazawa, Y.; Saito, K.; Sorai, M. *Chem. Phys. Lett.* **2002**, *352*, 348. (e) Awere, E. G.; Burford, N.; Mailer, C.; Passmore, J.; Schriver, M. J.; White, P. S.; Banister, A. J.; Oberhammer, M.; Sutcliffe, L. H. *J. Chem. Soc., Chem. Commun.* **1987**, 66.
(16) DTDAs: (a) Alberola, A.; Clarke, C. S.; Haynes, D. A.; Pascu, S. I.; Rawson, J. M. *Chem. Commun.* **2005**, 4726. (b) Alberola, A.; Less, R. J.; Pask, C. M.; Rawson, J. M.; Palacio, F.; Oliete, P.; Paulsen, C.; Yamaguchi, A.; Farley, R. D.; Murphy, D. M. *Angew. Chem., Int. Ed. Engl.* **2003**, *42*, 4782. (c) Banister, A. J.; Bricklebank, N.; Lavender, I.; Rawson, J. M.; Gregory, C. I.; Tanner, B. K.; Clegg, W.; Elsegood, M. R. J.; Palacio, F. *Angew. Chem., Int. Ed. Engl.* **1996**, *35*, 2533. (d) Brooks, W. V. F.; Burford, N.; Passmore, J.; Schriver, M. J.; Sutcliffe, L. H. *J. Chem. Soc., Chem. Commun.* **1987**, 69. (e) Bricklebank, N.; Hargreaves, S.; Spey, S. E. *Polyhedron* **2000**, *19*, 1163. (f) Barclay, T. M.; Cordes, A. W.; George, N. A.; Haddon, R. C.; Itkis, M. E.; Oakley, R. T. *Chem. Commun.* **1999**, 2269.

Table 1. Mulliken Atomic Spin Population, in Electrons, Computed by Doing UB3LYP and UHF Calculations Using the Aug-cc-pVTZ Basis Set on All Atoms As Implemented in GAMESS-US[a]

	C1	C2	N3	N4	N5	S6	S7	S8
UB3LYP	−0.0587	−0.0575	+0.0385	+0.0379	+0.5226	+0.1943	+0.1234	+0.1995
UHF	−0.1474	−0.1418	+0.0701	+0.0663	+0.8276	+0.1067	+0.1053	+0.1131

[a] The atomic numbering is that shown in Figure 1a.

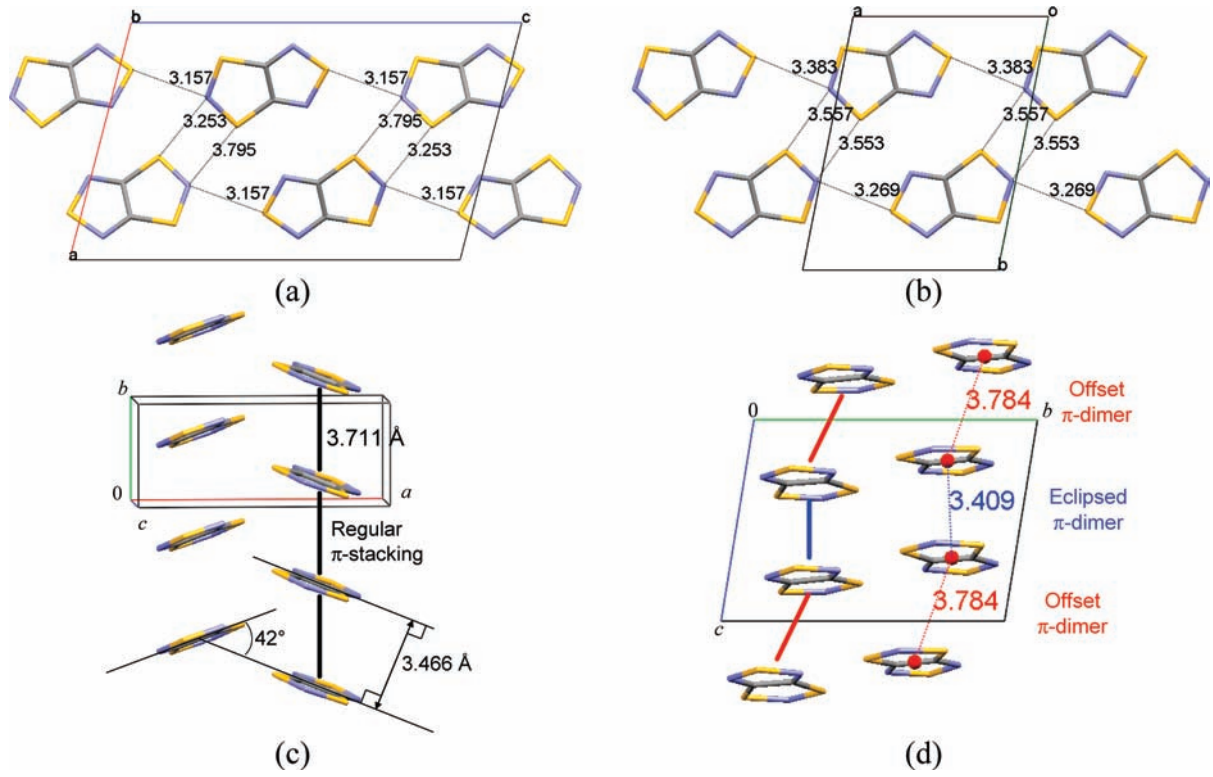

Figure 3. Packing of the monoclinic HT (SAXPOW05) and triclinic LT (SAXPOW06) crystal structures recorded at room temperature: planes perpendicular to the π stacks in the (a) HT (viewed down *b*) and (b) LT (viewed down $-c^*$) unit cells; π stacks in (c) HT (viewed along *b*) and (d) LT (viewed along *c*) phases. Selected head-to-tail S···N distances are given in a and b [S···N distances < 3.55 Å (within unit cell) and < 3.80 Å (stacks of layers)] and centroid···centroid distances in c and d.

of the radical···radical magnetic interactions present in the crystal. The four steps involved in the procedure are as follows.

(1) Analysis of the crystal structure to identify all unique, close radical···radical pairs present in the crystal. This analysis was carried out on both the monoclinic HT and the triclinic LT structures for each of the six SAXPOW01−06 crystal structures. All radical···radical pairs where the distance between their centroids[17] is shorter than 8 Å were considered in the analysis, after checking that this cutoff included all first nearest neighbors and the closest second nearest neighbors.

(2) Calculation of the radical···radical magnetic interactions (J_{AB}) for all unique pairs selected in the previous step. As is well established in the literature, the J_{AB} through-space magnetic interaction for a doublet pair of TTTA radicals can be obtained as $J_{AB} = [E_{BS}{}^{S} - E^{T}]$,[18] where the open-shell singlet is computed using the broken-symmetry approximation[19] and DFT/UB3LYP functional.[20,21] This expression assumes that the overlap between SOMO orbitals on radicals A and B is small, which is usually the case for through-space magnetic interactions. J_{AB} exchange couplings were also computed using a three-radical ABC model (i.e., a trimer) that would allow evaluation of the impact on the value of J_{AB} due to polarization caused by nearby radicals in comparison to using the corresponding isolated AB dimer model. The possible spin states in an ABC trimer are a quartet (HS, high-spin state) and three doublets (LS, low-spin state), where the spins are distributed as follows among the spin centers A, B, and C (see Figure 4): ααα (HS), $\beta\alpha\alpha$ (LS1), $\alpha\beta\alpha$ (LS2), and $\alpha\alpha\beta$ (LS3). The three possible pairwise J_{ij} (i, j = A, B, C) magnetic interactions can be calculated from the energies of these four states as indicated in eqs 1−3.

(17) Mercury software 4.2.1: Bruno, I. J.; Cole, J. C.; Edgington, P. R.; Kessler, M.; Macrae, C. F.; McCabe, P.; Pearson, J.; Taylor, R. *Acta Crystallogr.* **2002**, *B58*, 389.

(18) From the general Heisenberg Hamiltonian $\hat{H} = -2\sum_{A,B}^{N} J_{AB}\hat{S}_A \cdot \hat{S}_B$, for a pair of A and B radicals, the J_{AB} value is computed as the energy difference between biradical open-shell singlet S and triplet T states, $\Delta E^{S-T} = E^{S} - E^{T} = 2J_{AB}$. The expression chosen to compute the energy difference is $E^{S} - E^{T} = 2(E_{BS}^{S} - E^{T})/(1 + S_{ab})$. Open-shell singlet systems separate alpha spin density and beta spin density on different radicals. In our case, once the broken symmetry approximation is applied, the resulting overlap between the alpha SOMO and the beta SOMO is very small. Thus, those orbitals are localized on each of the two radicals. This leads to $S_{ab} \approx 0$. As a conclusion $J_{AB} = E_{BS}^{S} - E^{T}$.

(19) (a) Noodleman, L. *J. Chem. Phys.* **1981**, *74*, 5737. (b) Noodleman, L.; Davidson, E. R. *Chem. Phys.* **1986**, *109*, 131.

(20) Parr, E. G.; Yang, W. *Density Functional Theory*; Oxford University Press: New York, 1989.

(21) (a) Becke, A. D. *Phys. Rev. A* **1988**, *38*, 3098. (b) Becke, A. D. *J. Chem. Phys.* **1993**, *98*, 5648. (c) Lee, C.; Yang, W.; Parr, R. G. *Phys. Rev. B* **1988**, *37*, 785.

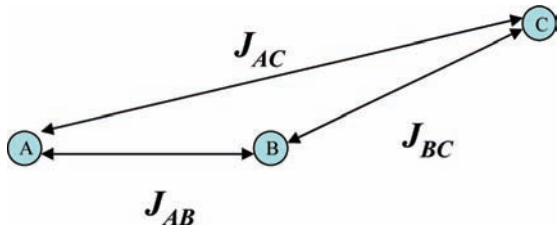

Figure 4. Schematic diagram of the trimeric ABC model used to calculate pairwise J_{ij} values.

$$E_{HS} - E_{LS1} = -(J_{AB} + J_{AC}) \quad (1)$$

$$E_{HS} - E_{LS2} = -(J_{AB} + J_{BC}) \quad (2)$$

$$E_{HS} - E_{LS3} = -(J_{BC} + J_{AC}) \quad (3)$$

The values of E_{HS}, E_{LS1}, E_{LS2}, and E_{LS3} were first computed by doing UB3LYP[21] calculations. Multireference many-body second-order perturbational (MRMBPT2[22]) calculations were done for some J_{AB} magnetic interactions to confirm the UB3LYP results. Note that in MRMBPT2 calculations J_{AB} is given as half of the difference between the lowest energy open-shell singlet state and the lowest energy triplet state [that is, $J_{AB} = (E^S - E^T)/2$].[23]

(3) Determination of the magnetic topology of the crystal described by the non-negligible J_{AB} magnetic interactions and finite minimal magnetic model. The minimal magnetic model comprises the smallest group of radicals whose propagation along the three crystallographic axes reproduces the magnetic topology of the infinite crystal in an even way. It should include all significant J_{AB} magnetic interactions in proportions as close as possible to those found in the infinite crystal. Larger models can also be obtained by extending the minimal magnetic model. However, if the minimal magnetic model is properly defined the macroscopic properties computed as it is enlarged should converge toward the experimental data.

(4) Calculation of the macroscopic magnetic properties of the crystal from the full energy spectrum obtained by diagonalization of the matrix representation of the appropriate Heisenberg Hamiltonian. The matrix representation of the Heisenberg Hamiltonian (eq 4) in the space of all eigenstates of the minimal magnetic model space is uniquely defined when the values for all J_{AB} values are computed. These values are computed in step 2, and the model space is defined in step 3.

$$\hat{H} = -2\sum_{A,B} J_{AB}\hat{S}_A \cdot \hat{S}_B \quad (4)$$

The size of the matrix representation increases with the number n of doublet radical centers as $n!/[(n/2)!(n/2)!]$. In practice, this means that we are limited to models of 16 spin centers or fewer. Finally, it is worth pointing out here that, for reasons of code implementation, we used the following form of the Heisenberg Hamiltonian (eq 5), which results in the same energy differences between eigenvalues as those obtained using the more common expression given in eq 4. The energy spectrum of a given magnetic space is the relevant parameter for obtaining the macroscopic properties of interest.

$$\hat{H} = -2\sum_{A,B} J_{AB}\left(\hat{S}_A \cdot \hat{S}_B + \frac{1}{4}\hat{I}_{AB}\right) \quad (5)$$

The magnetic susceptibility curve computed using eigenvalues obtained from eq 4 or 5 is the same, and this is also true for any other macroscopic magnetic property (heat capacity, magnetization, etc.). Note that in eqs 4 and 5, $\hat{S}_A$ and $\hat{S}_B$ are the total spin operators acting on radicals A and B and $\hat{I}_{AB}$ is the identity operator.

The procedure described above is called *bottom-up* because the macroscopic magnetic properties are obtained from the microscopic radical···radical magnetic interactions without any prior assumptions as to the type of mechanism acting between the radicals of the crystal. It is a first-principles procedure because the J_{AB} magnetic interaction for each pair is obtained from energy differences between states computed by first-principles methods (high-level ab initio[24] or DFT methods[20]). The DFT calculations were carried out using the B3LYP functional[21] implemented in GAUSSIAN03[25] and the following three basis sets in order of increasing quality: 6-31+G(d),[26] Aug-cc-pVDZ,[27,28] and Aug-cc-pVTZ.[27,29] The largest basis set was found to be necessary to obtain an accurate determination of the magnetic exchange mechanism in the monoclinic HT phase (see below). Multireference many-body MRMBPT2[22] calculations were performed using GAMESS-US[30] program with 6-31+G(d) and Aug-cc-pVDZ basis sets.

Results and Discussion

1. Comparative Analysis of the High- and Low-Temperature Crystal Structures of TTTA. As already mentioned, six crystal structures have been published for the TTTA radical (Table 2 gives unit cell parameters).[3−5,7,31] These six structures can be grouped into two families of structures according to the polymorph type (namely, monoclinic HT and triclinic LT) that share the same packing and show small changes in the intermolecular distances due to thermal expansion. These thermal effects are the cause of the contraction of the *a*, *b*, and *c* cell parameters when the temperature decreases. We describe below the main features of these two families of structures of TTTA, focusing only on the most relevant differences.

TTTA is a rigid planar molecule whose SOMO electron resides in a π^* orbital delocalized over both five-membered rings (Figure 1b). It crystallizes on vacuum sublimation at just above room temperature as a mixture of crystals of the HT (mono-

(22) (a) Wolinski, K.; Sellers, H. L.; Pulay, P. *Chem. Phys. Lett.* **1987**, *140*, 225. (b) Hirao, K. *Int. J. Quantum Chem. Symp.* **1992**, *26*, 517. (c) Nakano, H. *J. Chem. Phys.* **1993**, *99*, 7983.
(23) At the MRMBPT2 level, $\Delta E^{S-T} = E^S - E^T = 2J_{AB}$ and thus $J_{AB} = (E^S - E^T)/2$.
(24) Szabo, A.; Ostlund, N. S. *Modern Quantum Chemistry*; Macmillan: New York, 1982.
(25) Frisch, M. J.; et al. *Gaussian 03*, Revision C.02; Gaussian, Inc.: Wallingford, CT, 2004.
(26) 6-31+G(d) split-valence basis set: (a) Hariharan, P. C.; Pople, J. A. *Theor. Chim. Acta* **1973**, *28*, 213. (b) Francl, M. M.; Petro, W. J.; Hehre, W. J.; Binkley, J. S.; Gordon, M. S.; DeFrees, D. J.; Pople, J. A. *J. Chem. Phys.* **1982**, *77*, 3654.
(27) (a) Dunning, Jr., T. H. *J. Chem. Phys.* **1989**, *90*, 1007. (b) Kendall, R. A.; Dunning, Jr., T. H.; Harrison, R. J. *J. Chem. Phys.* **1992**, *96*, 6796. (c) Woon, D. E.; Dunning, Jr., T. H. *J. Chem. Phys.* **1993**, *98*, 1358.
(28) Aug-cc-pVDZ basis set contraction for C and N (10s,5p,2d) → [4s,3p,2d] and for S (13s,9p,2d) → [5s,4p,2d].
(29) Aug-cc-pVTZ basis set contraction for C and N (11s,6p,3d,2f) → [5s,4p,3d,2f] and for S (16s,10p,3d,2f) → [6s,5p,3d,2f].
(30) Schmidt, M. W.; Baldridge, K. K.; Boatz, J. A.; Elbert, S. T.; Gordon, M. S.; Jensen, J. H.; Kosecki, S.; Matsunaga, N.; Nguyen, K. A.; Su, S. J.; Windus, T. L.; Dupuis, M.; Montgomery, J. A. *J. Comput. Chem.* **1993**, *14*, 1347.
(31) Clarke, C. S.; Jornet, J.; Deumal, M.; Novoa, J. J. *Polyhedron* **2009**, *28*, 1614.

Table 2. Unit Cell Data for the Six Published Data Sets of TTTA[a]

	T (K)	unit cell volume (Å^3)	a	b	c	α	β	γ	ref
				HT monoclinic $P2_1/c$					
SAXPOW04	225	502.66	9.4280	3.6650	15.0290		104.545		3
SAXPOW03	250	505.37	9.4320	3.6810	15.0400		104.577		3
SAXPOW05	RT	510.80	9.4440	3.7110	15.0630		104.628		5
SAXPOW02	310	511.60	9.4430	3.7170	15.0630		104.615		3
				LT triclinic $P\bar{1}$					
SAXPOW01	150	494.17	6.9220	7.4920	9.9690	77.564	79.209	83.048	3
SAXPOW06	RT	507.20	7.5310	10.0230	7.0240	100.598	96.978	77.638	5

[a] Note the different axis settings for the two triclinic data sets. Refcodes SAXPOW01-06 given by CCDC.[6]

Table 3. Changes in the π Dimer Interatomic Separations (d) and Relative Orientation (θ) of the Six Crystal Structures of TTTA on Changing Temperature[a]

	Monoclinic				Triclinic	
Code	SAXPOW04	SAXPOW03	SAXPOW05	SAXPOW02	SAXPOW01	SAXPOW06
T (K)	225	250	RT	310	150	RT
d (Å)	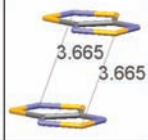	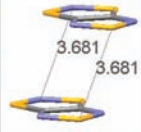	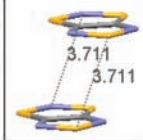	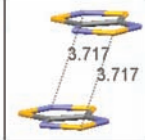	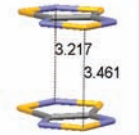	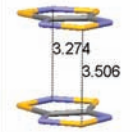
θ(°)	69.47	69.28	69.05	69.02	90.31 / 88.70	91.03 / 89.41
mean θ					89.51	90.22

[a] θ is the angle taken along the central C1−C2 bond in one radical and then to the C2 atom of the second radical (see Figure 1a for atom numbering). Note that θ (and also d) in the monoclinic π dimer has one value since the mean molecular planes of the two radicals are parallel. Instead, in the triclinic π dimer, θ has two values due to the fact that the mean molecular planes show an angle of 3.4° between both radicals.

clinic) and LT (triclinic) polymorphs. The two polymorphs contain planes of radicals that π stack in the third dimension (see Figure 3). The polymorphs present similar packing motifs in these 2D planes, and adjacent radicals are linked by a rhombohedral network of lateral S···N short contacts (Figures 3a and 3b). These contacts, which are very common in thiazyl radicals,[32] are expected to be energetically stable (as otherwise the crystal would collapse) and driven by a combination of lone-pair S···N dispersion interactions tuned by the dipole···dipole interaction which arises from the strong TTTA dipole moment (shown in Figure 1d). The main difference between the HT and the LT crystal packing resides in the way these planes stack in the third dimension, which leads on from the molecules not lying completely flat within their 2D planes. In the HT monoclinic structure the π stacking of planes is regular, i.e., radicals within a stack are parallel and equally spaced (at 3.711 Å, Figure 3c). However, between HT neighboring π stacks, the TTTA radicals are at a slight angle to each other, i.e., radicals in adjacent stacks are tilted 42° (Figure 3c). In contrast, in the LT triclinic structure (Figure 3d), each π stack shows pairs of nearly eclipsed radicals (shortest intrapair distance of 3.409 Å) separated from the next nearly eclipsed π dimer by 3.784 Å. In this case, LT neighboring π stacks show adjacent radicals tilted by 3° (Figure 3d). A further difference comes from the fact that the asymmetric unit of the HT monoclinic and LT triclinic polymorphs contains one and two radicals, respectively. This means that adjacent radicals in the π stack are not symmetrically equivalent in the LT triclinic phase.

(32) (a) Rawson, J. M.; Banister, A. J.; Lavender, I. *Adv. Het. Chem.* **1995**, *62*, 137. (b) Clarke, C. S.; Haynes, D. A.; Smith, J. N. B.; Batsanov, A. S.; Howard, J. A. K.; Pascu, S. I.; Rawson, J. M. *CrystEngComm* **2010**, *12*, 172.

It should be noted that differences between the data sets for the same polymorph recorded at different temperatures are manifested only in slight alterations in unit cell parameters (see Table 2) due to thermal expansion/contraction, and no great change is observed. Thermal expansion induces slight changes in the relative position of the radicals in the stacks. The most relevant changes during the thermal progression are the intermolecular separation (d) and relative position (θ) of the two molecules within the π dimer, whose values are collected in Table 3. The smooth variation of θ indicates that there is no change in the packing patterns until the LT → HT phase change occurs, when there is an abrupt jump. Within each phase there are only slight alterations in separation caused by thermal expansion.

2. Nature of the Magnetic Interactions in the Low- and High-Temperature Phases of TTTA. No exhaustive studies including all possible radical···radical pairs have previously been reported on the mechanism of the magnetic interaction of the monoclinic HT and triclinic LT phases of the TTTA molecule-based system. This fact prompted us to apply the First-Principles Bottom-Up procedure[12] to get a sound evaluation of the changes in the distribution of magnetic interactions in these two phases of TTTA. The room-temperature SAXPOW05 and SAXPOW06 crystals were selected as representatives of the HT and LT families, respectively (see Table 2).[5]

Analysis of the monoclinic HT SAXPOW05 structure of TTTA (step 1 of our procedure[12]) indicates that there are 11 unique close radical···radical pairs whose centroid···centroid distance is smaller than 8.0 Å (this cutoff includes all first neighbors and the closest second neighbor pairs). Table 4 collects the main geometrical data defining the relative orientation of these 11 unique pairs, whose position in the HT crystal

Table 4. Main Structural Data for the Unique Close Pairs in the Room-Temperature Monoclinic HT (^{M}) and Triclinic LT (^{T}) Structures of TTTA Crystal (SAXPOW05 and SAXPOW06)[a]

Monoclinic HT (SAXPOW05)				Triclinic LT (SAXPOW06)			
Pair	centroid separation (Å)	shortest atom-atom contact (Å)	between atoms	Pair	centroid separation (Å)	shortest atom-atom contact (Å)	between atoms
A^M1	3.711	3.566	S···N (π)	A^T1	3.409	3.274	N···N (π)
A^M2	7.422	6.935	S···N (π)	A^T2	3.784	3.442	S···N (π)
				A^T3	7.024	6.885	S···N (π)
B^M1	5.813	3.395	S···S (twist)	B^T1	5.886	3.277	S···S (lat)
B^M2	7.832	6.251	S···S (twist)	B^T2	5.912	3.349	S···S (π)
				B^T3	7.588	5.737	S···S (lat)
				B^T4	6.511	5.314	S···N (π-offset)
				B^T5	7.453	4.592	S···S (lat)
C^M1	7.548	3.157	S···N (twist)	C^T1	7.531	3.269	S···N (lat)
				C^T2	7.531	3.383	S···N (lat)
				C^T3	7.538	3.402	S···N (lat)
D^M1	5.168	3.560	S···N (π)	D^T1	5.112	3.724	S···N (π)
D^M2	5.516	3.048	S···N (lat)	D^T2	6.420	4.517	S···N (lat)
D^M3	7.109	6.598	S···S (π)	D^T3	5.417	2.952	S···N (lat)
				D^T4	6.381	4.439	S···N (lat)
				D^T5	6.381	4.439	S···N (π-offset)
				D^T6	7.804	6.865	S···N (π)
				D^T7	7.823	5.658	N···N (lat)
E^M1	7.147	3.253	S···N (twist)	E^T1	6.890	3.230	S···N (lat)
				E^T2	7.202	3.517	S···N (lat)
				E^T3	7.212	3.553	S···N (lat)
F^M1	6.734	3.132	S···N (lat)	F^T1	6.656	3.088	S···N (lat)
F^M2	7.004	4.097	S···N (lat)	F^T2	7.121	4.084	S···N (π-offset)
				F^T3	7.492	4.659	S···N (lat)
				F^T4	7.464	4.683	N···N (lat)

[a] One color is given to each of the significant J_{AB} couplings within the π stack (A) and between π stacks (B−F). When more than one radical−radical pair is found for the same relative orientation but they differ geometrically, they are distinguished by a number after the letter name and a change in the color code. The coloring and labeling methodology is common to both monoclinic and triclinic structures to aid comparison. The resulting radical pairs are common to all four monoclinic (SAXPOW02-05) and both triclinic (SAXPOW01,06) crystal structures.

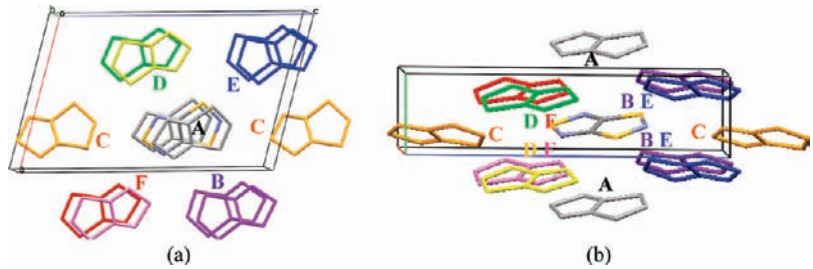

Figure 5. View of the 11 unique radical···radical pairs found in the monoclinic HT crystal structure of TTTA having a centroid···centroid distance shorter than 8 Å (a) down the π stack and (b) perpendicular to the π stack. Each pair is labeled by a letter (A−F in Table 4) that identifies its relative position in the crystal.

is shown in Figure 5 using the same color coding as employed in Table 4. The lower symmetry of the triclinic LT SAXPOW06 structure of TTTA, with two molecules in the asymmetric unit, results in the existence of 26 unique close radical···radical pairs having a centroid···centroid distance shorter than 8.0 Å (Table 4). Figure 6 shows the 12 nearest neighbors around a central radical in the triclinic structure. Note that there are two sets of arrangements for the triclinic structure as there are two possible 13-radical clusters since either one of the two nonsymmetry-equivalent molecules can be at the center and these two options give different sets of pairs (see Figure 6).

In both polymorphs (Table 4), the pairs within the π stacks are labeled A and the spokes connecting the π stacks are given a letter each (B−F, note there are only 5 symmetry unique spokes, not 6, as C is repeated, see Figures 5 and 6). When more than one radical···radical pair is found for the same relative orientation but they differ geometrically, they are distinguished by a number after the letter name and a change in the color coding (e.g., A^M1, A^M2). For a better visualization of the radical arrangement, there are two views down (Figures 5a, 6a, and 6c) and perpendicular to (Figures 5b, 6b, and 6d) the π stack. Notice that the central radical in all A−F pairs is marked in yellow−gray−blue atomic colors (yellow denotes S, gray C, and blue N).

3. Comparative Study of the Magnetic Interactions in the HT and LT Polymorphs of TTTA. The value of all J_{AB} radical···radical exchange couplings was computed using the crystal geometry (step 2 of our procedure[12]) using the UB3LYP functional and the broken-symmetry approach to describe the open-shell singlet state of the pairs. Note that triplet and broken-symmetry singlet orbitals are all of π symmetry, in agreement with the doublet SOMO shown in Figure 1b. For the monoclinic (HT) structure, the J^M_{AB} parameters were calculated for all 11 unique radical···radical pairs identified above and for the four

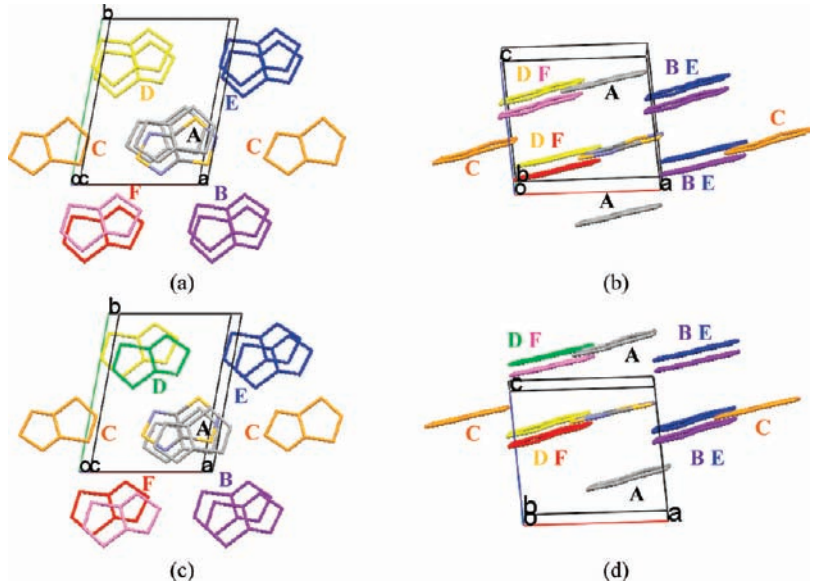

Figure 6. View of the 26 unique radical···radical pairs found in the triclinic LT crystal structure of TTTA down the π stack (a and c) and perpendicular to the π stack (b and d), having a centroid···centroid distance smaller than 8 Å. Notice there are two TTTA molecules in the asymmetric unit, and thus, there are two different central radicals, seen here in in yellow-gray-blue atomic colors, which give rise to two differently arranged clusters.

Table 5. Values of All J_{AB} Parameters (in cm^{-1}) Calculated at the UB3LYP Level with 6-31+G(d)|Aug-cc-pVTZ Basis Sets for the Unique Radical···Radical Pairs Found in the Monoclinic (^{M}, HT) and Triclinic (^{T}, LT) Structures Obtained at the Indicated Temperature, T[a]

	T									T			
Pair	225 K SAXPOW04		250 K SAXPOW03		Room Temp SAXPOW05		310 K SAXPOW02		Pair	150 K SAXPOW01		Room Temp SAXPOW06	
basis set	6-31+ G(d)	aug-cc-pVTZ	6-31+ G(d)	aug-cc-pVTZ	6-31+ G(d)	aug-cc-pVTZ	6-31+ G(d))	aug-cc-pVTZ		6-31+ G(d)	aug-cc-pVTZ	6-31+ G(d)	aug-cc-pVTZ
A^M1	-175.01	-199.92	-160.59	-183.76	-135.61	-155.63	-134.23	-154.11	A^T1	-2020.09	-2261.09	-1755.01	-1967.32
A^M2					-0.09				A^T2	-51.93		-50.15	
									A^T3	-0.20		-0.15	
B^M1	+11.24			+9.88	+10.69	+9.48			B^T1	+14.38		+12.42	
B^M2					-0.24				B^T2	+7.22		+6.10	
									B^T3	-0.99		-1.01	
									B^T4	-0.83		-0.70	
									B^T5	+0.15		+0.15	
C^M1	-8.56			-8.86	-8.12	-8.54			C^T1	+2.61		+2.24	
									C^T2	+1.38		+1.32	
									C^T3	+1.23		+1.14	
D^M1	+6.36			+6.50	+5.77	+5.62			D^T1	+4.26		+4.13	
D^M2	-2.00			-0.89	-1.95	-0.79			D^T2	+0.26		+1.58	
D^M3					-0.11				D^T3	-5.62		-4.63	
									D^T4	+0.26		-1.08	
									D^T5	+0.29		+0.26	
									D^T6	-0.08		-0.11	
									D^T7	0.00		+0.02	
E^M1	+2.44			+2.65	+2.33	+2.62			E^T1	-19.38		-15.87	
									E^T2	+4.59		+4.04	
									E^T3	+4.26		+3.45	
F^M1	-1.84			-1.45	-1.71	-1.37			F^T1	-2.50		-2.15	
F^M2	+0.48			+0.75	-1.69	-1.36			F^T2	+0.83		+0.70	
									F^T3	+0.02		+0.02	
									F^T4	-0.02		0.00	

[a] The refcode given to each structure is also indicated.

different temperatures at which the struture has been recorded (see Table 5). The calculation was done at the UB3LYP/6-31+G(d) and UB3LYP/Aug-cc-pVTZ levels. Similarly, for the triclinic (LT) structure, the J^T_{AB} parameters were calculated for all 26 unique radical···radical pairs identified above and for the two known crystals that belong to this phase (RT and 150

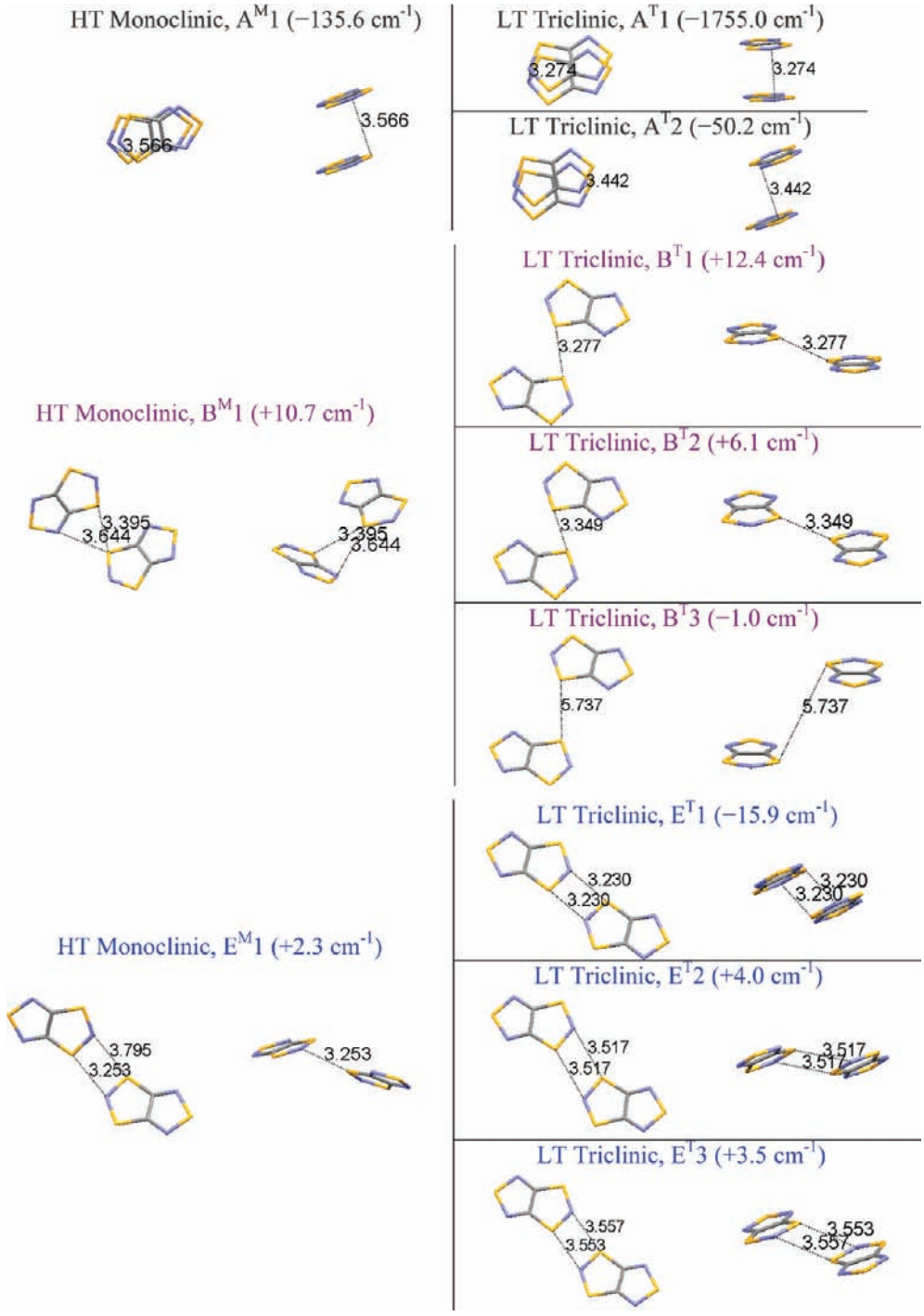

Figure 7. Dimer geometries of selected pairs in the monoclinic SAXPOW05 HT (A^M1 and B^M1, left) and triclinic SAXPOW06 LT (A^T1, A^T2, B^T1, and E^T1, right) phases with $|J_{AB}|$ being larger than 10.0 cm^{-1}. Note that for a better geometry comparison and visualization of the HT ↔ LT crystal transformation we listed all B and E pairs. All distances are in angstroms.

K in Table 5). On the basis of previous experience,[33] only those pairs with $|J_{AB}| > 1.0$ cm^{-1} were taken as significant in this study. Notice that the values are grouped according to where they are found in the crystal structure for an easier comparison between monoclinic and triclinic structures (A, B, C, etc.). Among these pairs, there are 8 significant J^M_{AB} couplings in the monoclinic HT structure, as described in our preliminary report,[31] and 16 significant J^T_{AB} couplings in the triclinic LT structure, whose $|J_{AB}|$ is larger than 1.0 cm^{-1}. Monoclinic and triclinic crystals thus show very different sets of J_{AB} parameters due to the higher symmetry of the monoclinic space group.

It is worth noting the much larger size of $J(A^T1)$ with respect to any of the other exchange parameters in both triclinic LT and monoclinic HT crystals, irrespective of the temperature (see

(33) The number of significant digits we have in the energy of the high- and low-spin states gives an accuracy of |0.05| cm^{-1}, which is provided by the cutoffs employed in the computation of the integrals and in the self-consistent process. For simulation purposes, it has been proved that J_{AB} values smaller than 1% of the largest computed J_{AB} value do not contribute in statistical mechanics calculations. Thus, for the monoclinic crystals, a cutoff of 1.0 cm^{-1} has been chosen since the largest J_{AB} is ∼100 cm^{-1}. For the triclinic structures, a cutoff of 1.0 cm^{-1} has been also chosen to be consistent with the monoclinic cutoff.

Table 5). In the room-temperature (RT) HT crystal, $J(A^M1)$ is -135.6 cm^{-1}, with the next biggest coupling being $+10.7$ cm^{-1}. In the room-temperature LT structure, $J(A^T1)$ is -1755.0 cm^{-1}, with the next in terms of size being -50.2 cm^{-1}. Note that the groups of dimers of the triclinic structure shown in Table 5 all appear to transform into a single pair on the phase change to the monoclinic structure. There is no direct experimental observation of this, but this conclusion is reached by inspection of the symmetry and patterns of the two crystal structures and comparison of molecular positions. It then follows that small differences in separations and angles of approach for corresponding pairs in the HT and LT crystals lead to considerable differences in J_{AB} values. These changes can be monitored with the help of Figure 7, which associates the radical pairs showing $|J_{AB}| > 10.0$ cm^{-1} in triclinic LT with those in monoclinic HT for the room-temperature structures (SAXPOW06 and SAXPOW05, respectively). The most important J_{AB} difference is found in A1, whose dimer radicals change orientation from a parallel offset π dimer at 3.711 Å (A^M1 in Table 3, Figures 3c and 7, which varies from -135.6 in HT to -1755.0 cm^{-1} in LT, due to a change in the distance) to a nearly eclipsed π dimer with radicals 3.409 Å apart (A^T1 in Table 3, Figures 3d and 7). The next most important variation in terms of the magnetic analysis is found in the A^T2 pair, which also correlates with A^M1 and goes from -135.6 cm^{-1} in HT to -50.2 cm^{-1} in LT. In fact, one can easily interconvert A^T2 into A^M1, which can also become A^T1 (see Supporting Information Figure S1). Next in relevance come the changes in E^T1, E^T2, and E^T3 LT pairs (-15.9, $+4.0$, and $+3.5$ cm^{-1}), all correlating with E^M1 ($+2.3$ cm^{-1}), followed by the B^T1, B^T2, and B^T3 LT pairs ($+12.4$, $+6.1$, and -1.0 cm^{-1}), which correlate with B^M1 in HT ($+10.7$ cm^{-1}) (see Figure 7). The three C pairs in LT go from $+2.2$, $+1.3$, and $+1.1$ to -8.1 cm^{-1} in HT, while the set of D pairs go from $+4.1$, $+1.6$, -4.6, and -1.1 to $+5.8$ and -2.0 cm^{-1} (see Supporting Information Figures S2−S3). Finally, the F pairs in LT (-2.2 and $+0.7$ cm^{-1}) correlate with the two F pairs in HT (both -1.7 cm^{-1}).

Comparison of Tables 4 and 5 shows that (a) there is no correlation between the values of J_{AB} and the shortest atom···atom or centroid···centroid distances (see A^T1 and B^T1 whose shortest atom···atom distance is practically the same or C^M1 and C^T1 whose centroid separation is very similar but whose J_{AB} values differ significantly; also compare C^M1 and D^M1, the pair with the largest centroid separation has the largest J_{AB} in absolute value), (b) the variation of J_{AB} with temperature but within the same phase (monoclinic or triclinic) is small and the sign of the magnetic interaction does not change, and (c) the magnitude of J_{AB} increases on cooling, which is consistent with thermal contraction shortening the inter-radical distances and thus allowing better orbital overlap. Also, according to Table 5, there is no change in the sign or order of magnitude of the UB3LYP-computed J_{AB} results when the 6-31+G(d) basis set is substituted by the much better Aug-cc-pVTZ basis ($|J_{AB}|$ at the 6-31+G(d) level is systematically 15% and 12% smaller than that at the Aug-cc-pVTZ level for monoclinic and triclinic structures, respectively). By comparing the UB3LYP/Aug-cc-pVDZ and UB3LYP/Aug-cc-pVTZ results (Table 6) one can conclude from the smooth progression that the larger basis set results are close to the basis set limit for UB3LYP calculations. Note also that the largest magnetic exchange couplings (A^T1 and A^M1 in Table 6) agree closely with previously published J_{AB} values that were found by fitting experimental data to a 1D Heisenberg chain model with interchain exchange described by a mean field term in the monoclinic case and to the Bleaney−Bowers expression for an exchange-coupled dimer of $S = 1/2$ ions in the triclinic case.[3,4]

Table 6. J_{AB} Values for the Closest π Dimer in the Triclinic (data set recorded at RT, SAXPOW06) and Monoclinic (RT, SAXPOW05) Structures Calculated Using DFT/UB3LYP and MRMBMP2 Methods and Different Basis Sets, Compared to the Fitted Values

method	SAXPOW06, $J(A^T1)$ /cm^{-1}	SAXPOW05, $J(A^M1)$ /cm^{-1}	ref
DFT/6-31+G(d)	−1755.01	−135.61	this work
DFT/Aug-cc-pVDZ	−1907.34	−148.98	this work
DFT/Aug-cc-pVTZ	−1967.32	−155.63	this work
MRMBMP2/6-31+G(d)	−1745.89		this work
MRMBMP2/Aug-cc-pVDZ	−2109.40		this work
fitted experimental data	−1440	−222	3

In the monoclinic HT TTTA crystal, the computed value for $J(A^M1)$ is -135.6 cm^{-1}, which is within the usual range for strong J_{AB} pairwise magnetic interactions. However, in the triclinic LT case, the value of $J(A^T1)$ ranges between -1700 and -1900 cm^{-1}, which is beyond the values usually published for this kind of purely organic system. Also, we found A^T1 to be an antiferromagnetically coupled open-shell singlet, instead of the generally assumed closed-shell ground state. Thus, the validity of the UB3LYP results for A^T1 was further checked by doing high-level ab initio multireference second-order perturbation (MRMBPT2) calculations,[22] using a 10 orbital and 10 electron active space and the 6-31+G(d) and Aug-cc-pVDZ basis set (Table 6). The computed MRMBPT2 value for $J(A^T1)$ is nearly identical to the UB3LYP result computed using the same basis (Table 6), which confirms the goodness of the DFT/UB3LYP level of theory.

All previous J_{AB} values were computed on isolated dimers. In order to check for possible polarization effects in computing J_{AB} magnetic interactions, they were also calculated using trimolecular clusters (Figure 4) for the room-temperature HT and LT structures (SAXPOW05 and SAXPOW06, respectively) at the UB3LYP/6-31+G(d) level. If polarization effects are important, the pairwise values of J_{AB}, J_{BC}, and J_{AC} computed using a trimolecular cluster should be significantly different than those computed as isolated dimers. In the triclinic LT structure, the pairwise J_{AB}, J_{BC}, and J_{AC} interactions computed with the trimer model gave -1761.3, -51.4, and -8.5 cm^{-1}, compared with -1755.0, -50.2, and -0.2 cm^{-1} using isolated radical pairs. The difference in the couplings between terminal radicals (-8.5 and -0.2 cm^{-1}) might perhaps be considered significant were they the magnetic couplings of an isolated pair calculated under different circumstances. However, in this context these couplings are both dwarfed by the large -1760 and -50 cm^{-1} J values which are also part of the magnetic topology via which the couplings were calculated and which are consistent in both dimer and trimer calculations. Therefore, the -8.5 and -0.2 cm^{-1} couplings are considered to be negligible in this context. The same analysis when performed for the monoclinic HT structure gave no significant change in the pair-calculated J_{ij} coupling in the π-stacking direction (J_{AB}, J_{BC}) and again a negligible 'outer' J_{AC} value between terminal radicals (-0.4 cm^{-1}). These results indicated that the isolated dimer model is correct and sufficient for the crystals under study in this work.

The non-negligible J_{AB} interactions create a network of interactions, called the magnetic topology (step 3 of our procedure,[12] see Figure 8a for monoclinic HT and Figure 8b for triclinic LT), where black dots correspond to the calculated

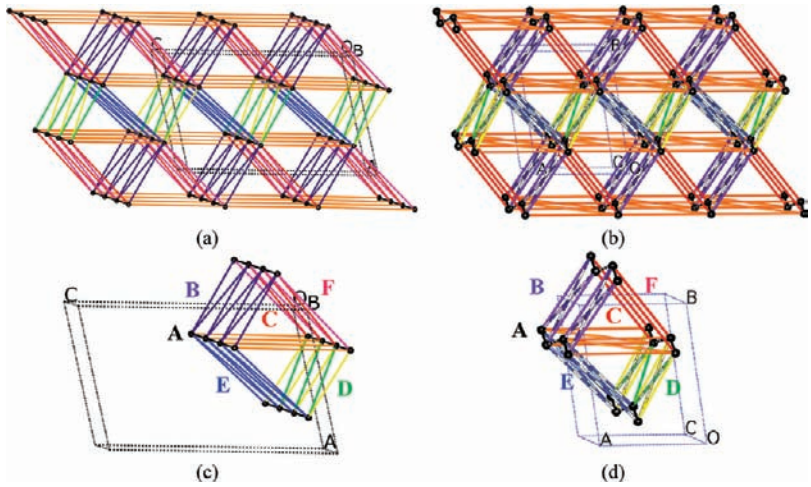

Figure 8. 3D magnetic topologies for the two phases of TTTA: (a) monoclinic HT and (b) triclinic LT. Small model extracted from the infinite topology of each structure to illustrate the connectivity of the *J* couplings and the correspondence with the pair labeling used in the tables above. These models each contain 16 spin sites and are called $4-4s^{M}$ and $4-4s^{T}$ (they comprise 4 chains each of 4 spins). Black dots denote the calculated centroids of the TTTA dimers. The colored lines represent the pairwise *J* couplings.

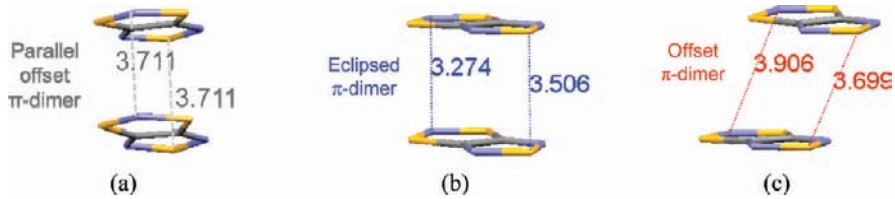

Figure 9. Three RT π pairs with the largest *J* couplings (see also Figure 7). (a) Parallel offset pair $A^{M}1$ in monoclinic structure. (b) Nearly eclipsed π-dimer pair $A^{T}1$ in the triclinic structure showing that molecular mean planes are not parallel. (c) Offset π pair $A^{T}2$ in the triclinic structure. For the latter two ($A^{T}1$, $A^{T}2$) the angle between mean planes is 3°.

centroids of the TTTA molecules. At first glance, the magnetic topologies of the HT and LT phases are similar: 1D chains of large *J* couplings (A-type pairs going into the page) that are linked quasi-hexagonally by weaker *J* magnetic interactions (in the plane of the paper). The use of data sets at different temperatures caused no alterations in these networks. However, small differences in separations and angles of approach for corresponding pairs in the HT and LT crystals lead to massive differences in J_{AB} values (as discussed above according to Figure 7). To summarize, the largest changes in size are produced within the chains, while the changes in the interchain magnetic interactions are much smaller but affect their magnitude and sign, making a qualitative estimate of their net effect impossible. This is not a drawback in the First-Principles Bottom-Up procedure as the net effect induced by all changes is evaluated exactly in the third step of this procedure.[12]

Given its leading role in the J_{AB} changes when going from the HT to the LT structure, the π-type overlap of TTTA molecules (A-type pairs) is easily the most important in terms of the overall magnetic behavior. As highlighted in Figure 9, the very large difference between the magnitudes of the strongest exchange couplings in each structure ($\sim$ 200 in monoclinic and $\sim$2000 cm^{-1} in triclinic, in absolute value) is due to relatively small changes in the pair geometry. In the monoclinic structure, the π pair (Pair $A^{M}1$, Figure 9a) comprises two parallel but offset molecules, and in the triclinic structure, the molecules in the closest π pair (pairs $A^{T}1-A^{T}2$, Figures 9b and 9c) are nearly eclipsed but not parallel (angle between mean planes is 3°) and are slightly closer together than in the monoclinic structure. Therefore, the change in the J_{AB}(A1) and J_{AB}(A2) parameters was further investigated. First, the effect of changing only the

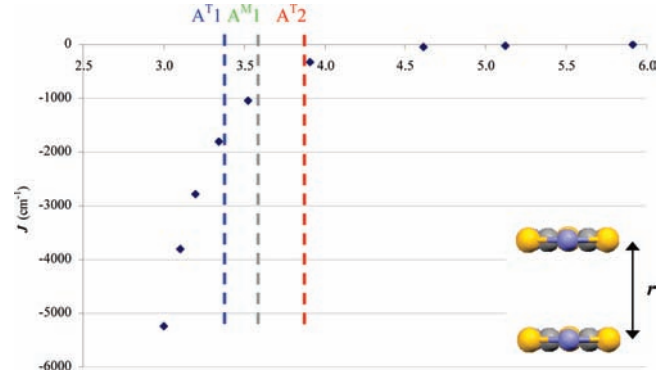

Figure 10. Dependence of J_{AB} value on varying the perpendicular separation (*r*, in angstroms) of a perfectly eclipsed π dimer. Note that the actual separation *r* inside the crystal of dimers $A^{T}1$ and $A^{T}2$ in triclinic SAXPOW06 and $A^{M}1$ in monoclinic SAXPOW05 is shown in dashed lines. All calculations are at the UB3LYP/6-31+G(d) computational level.

inter-radical distance in a parallel, eclipsed π dimer was considered (Figure 10a). As expected, the variation follows an exponential dependence (i.e., the further apart the molecules, the smaller the exchange coupling), and the scale of the J_{AB} change is notable. A comparison between the J_{AB} values calculated using crystal dimers $A^{T}1$ and $A^{T}2$ in the triclinic polymorph and $A^{M}1$ in the monoclinic (see dashed lines for inter-radical separation in Figure 10a) and perfectly eclipsed model dimers shows that J_{AB} is stronger when the two radicals are completely eclipsed: J_{AB} values computed using π dimers extracted from crystals are always smaller due to the effect of the lateral displacement. The importance of the degree of offset was also considered (Figure 11), using the dihedral angle θ as

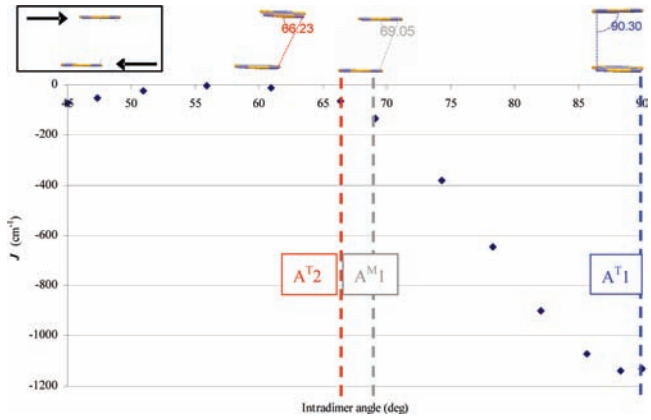

Figure 11. Sliding eclipsed molecules over each other starting from the perfect π dimer. The dependence of J_{AB} on the lateral displacement is measured in terms of the dihedral angle θ (in degrees, see text for definition), fixing the interplane distance at a value $r = 3.4$ Å (corresponding to monoclinic interplane separation) at the UB3LYP/6-31+G(d) computational level. The three figures are the three π pairs (A^M1, A^T1, A^T2) showing their degree of sliding θ for comparison at room temperature (see dashed lines for angle value).

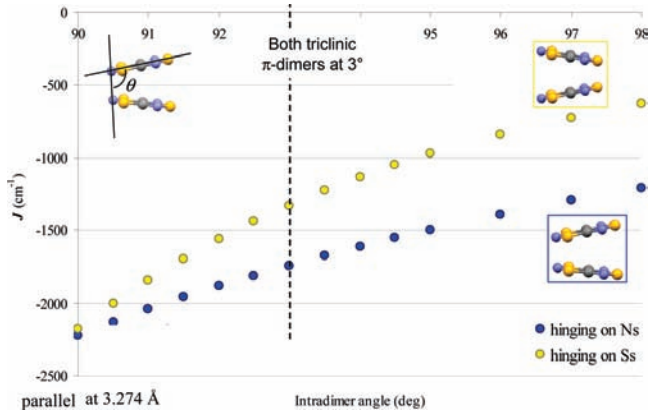

Figure 12. Dependence of J_{AB} on the angle of opening of the eclipsed π dimer where the starting structure is a perfectly parallel eclipsed π dimer with radicals at a perpendicular separation of 3.274 Å (at the UB3LYP/6-31+G(d) computational level).

a measure of the displacement (the angle of rotation of S8 of one radical of the dimer about the N4−S8 axis of the second radical, taking as reference the C2 atom of the same second radical) and starting from a perfectly eclipsed π pair ($\theta = 90°$) placed at an intermolecular distance of 3.4 Å (corresponding to A^T1). Figure 11 shows that although J_{AB} is again obviously largest at $\theta = 90°$, the sliding of one molecule over the other has a more complex dependence on J, which is thought to be due to the nonuniform nature of the SOMO, allowing different degrees of orbital overlap depending on exactly which parts of the nonbonding π-symmetry orbital (Figure 1b) are overlapping.

Finally, the angle of opening of a π-eclipsed pair is studied as we wished to check how important the 3° angle between mean planes is in the close A-type π dimer (Figure 12, the starting structure is at a separation of 3.274 Å corresponding to A^T1). The data show that the magnitude of J_{AB} decreases on increasing the angle between the two molecules. Note that J_{AB} decreases more slowly when it is the separation between sulfur atoms that is increasing (blue series in Figure 12) since S has a larger van der Waals radius than N. This suggests that better magnetic orbital overlap increases the strength of magnetic exchange, in agreement with previous observations.

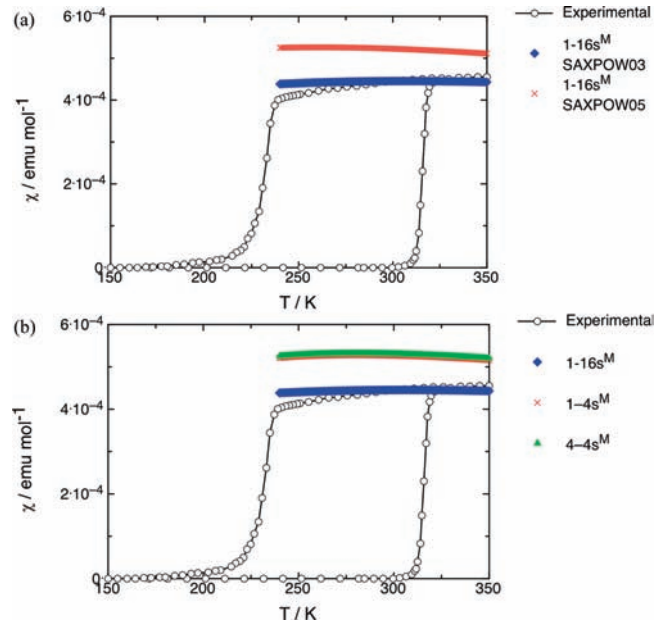

Figure 13. (a) Magnetic susceptibility as a function of temperature $\chi(T)$ for monoclinic HT crystal using structures determined at 250 K (SAXPOW03) and room temperature (SAXPOW05) employing a $1-16s^M$ magnetic model. The experimental curve[3] is also given to allow comparison (the HT results should be compared with the HT region of the experimental curve). (b) Comparison among $\chi(T)$ computed data using $1-16s^M$, $1-4s^M$, and $4-4s^M$ magnetic models. All calculations were done at the UB3LYP/Aug-cc-pVTZ level.

4. Reproducing the Bistability of Magnetic Susceptibility as a Function of Temperature. Once the magnetic topology of the monoclinic HT and triclinic LT crystals has been computed and rationalized, it is possible to select an appropriate finite minimal magnetic model space that evenly represents the magnetic topology of the infinite crystals. This space is required to calculate the matrix representation of the Heisenberg Hamiltonian, which is needed to obtain the full set of eigenvalues of that Hamiltonian, which is then employed to compute the magnetic susceptibility curve for the HT and LT crystals (step 4 of our procedure[12]). This computation can be done at any of the various temperatures at which the HT and LT polymorphs have been recorded, which allows the impact of thermal expansion on the computed magnetic susceptibility curves to be studied.

The impact of thermal expansion on the computed $\chi(T)$ for the monoclinic HT crystal structure has been tested using a variety of magnetic models (for instance, see Supporting Information Figure S4). Among these magnetic models, we have chosen the main magnetic motif, i.e., a 1D regular chain model with 16 radicals (namely, $1-16s^M$ model), with $J(A^M1) = -183.8$ and -155.6 cm^{-1} corresponding to SAXPOW03 (250 K) and SAXPOW05 (room temperature), respectively, for discussion. It has been observed that the experimental results are better reproduced using SAXPOW03 magnetic data at the UB3LYP/Aug-cc-pVTZ level (see Figure 13a and Supporting Information Figure S4 for a comparison between SAXPOW05/03 and between different basis sets). All monoclinic theoretical studies discussed from here on have been performed using SAXPOW03 data.

The $1-16s^M$ model is a purely 1D model, and the magnetic topology of the monoclinic HT crystal is clearly 3D (Figure 8). However, in spite of being 3D, the main motif of the magnetic topology of the HT polymorph consists of uniform AFM chains

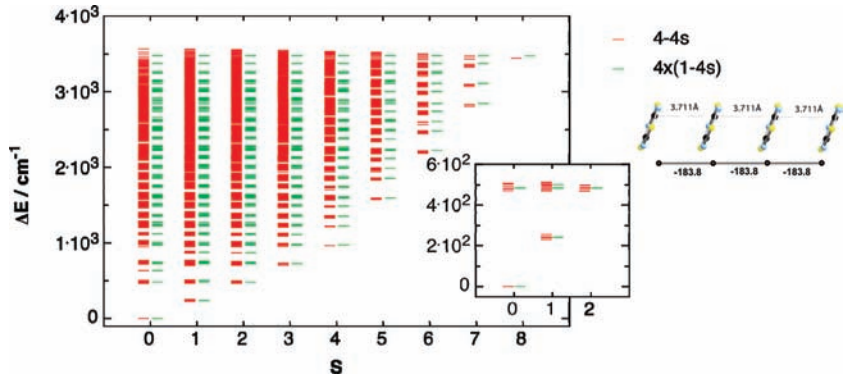

Figure 14. Energy spectra of all energy magnetic states found in the $4x(1-4s^M)$ and $4-4s^M$ magnetic models (i.e., 1D and 3D models, respectively) on the room-temperature monoclinic HT structure (SAXPOW05). See inset for $1-4s^T$ magnetic model, where the C···C distance in angstroms and $J(A^M1)$ in cm^{-1} are shown.

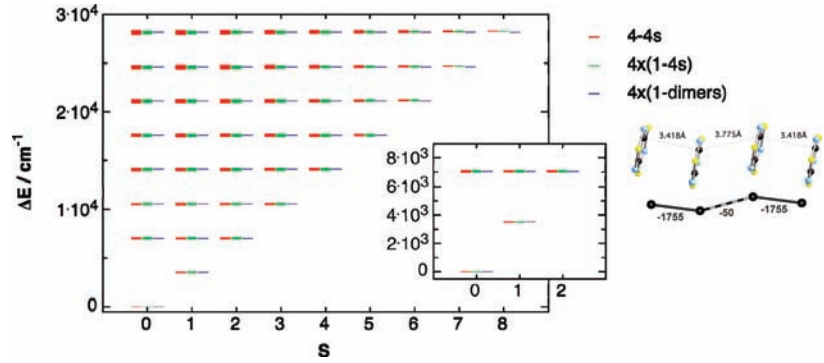

Figure 15. Energy spectra of all magnetic states found in the $4x(1\text{-dimers}^T)$, $4x(1-4s^T)$, and $4-4s^T$ magnetic models on the room-temperature triclinic LT structure (SAXPOW06) (i.e., 0D, 1D, and 3D magnetic models, respectively). See inset for $1-4s^T$ magnetic model, where the C···C distance in angstroms and $J(A^T1, A^T2)$ in cm^{-1} are shown.

($J(A^M1) = -183.8\ cm^{-1}$), well described by the 1D model, with weak interchain interactions giving rise to a very small ratio between inter- and intrachain magnetic interactions ($|J_{inter}| < 5\%\ |J_{intra}|$). In order to investigate the impact of including interchain interactions in the magnetic susceptibility of the HT crystal, the results obtained using an isolated $1-4s^M$ chain model and a 3D $4-4s^M$ magnetic model were compared (Figure 13b), since size limitations made comparison between the $1-16s^M$ and the $4-16s^M$ models impossible. The $4-4s^M$ results are slightly better than the data calculated for the $1-4s^M$ model, but the $1-16s^M$ magnetic model remains the model that most closely reproduces the experimental data (see Supporting Information Figure S5 for chain length discussion). Therefore, in the monoclinic HT region, the interchain magnetic interactions have almost no effect on the shape of the magnetic susceptibility curve (see Supporting Information Figures S6 and S7 for other models). A justification of this behavior can be obtained by looking at the lowest levels in the energy spectra of the magnetic eigenstates for a model using four isolated 4s chains [$4x(1-4s^M)$] and a $4-4s^M$ 3D model (Figure 14): the two spectra are nearly identical, which is consistent with the fact that the interchain magnetic interactions can be considered as a small perturbation of the 1D chain model and, consequently, the $4-4s^M$ spectrum is nearly identical to the $4x(1-4s^M)$ spectra, due to the small perturbation introduced by the interchain interactions.

In the triclinic LT case, irrespective of whether the data set used is that recorded at 150 K or at RT, all different magnetic model spaces selected give identical susceptibility curves. The magnetic topology of the LT crystal is dominated by the extremely large $J(A^T1)$ interaction ($-1755.0\ cm^{-1}$ in SAXPOW06), the remaining J_{AB} being <3% $J(A^T1)$. This large difference explains why the spectra of a 3D $4-4s^T$ magnetic model and a four isolated chain model, $4x(1-4s^T)$, are nearly identical and also why they are nearly indistinguishable compared with the energy spectra of four chains of noninteracting dimers ($4x(1\text{-dimers}^T)$, see Figure 15). This similarity results in a similar magnetic susceptibility curve for the $4-4s^T$, $4x(1-4s^T)$, and $4x(1\text{-dimers}^T)$ models. Therefore, when the J_{AB} values differ by orders of magnitude, the energy spectrum is dominated by the largest J_{AB} magnetic interaction and the smaller J_{AB} pairs just induce a small perturbation. In these cases, a 3D magnetic topology shows the same magnetic susceptibility curve as a 1D or 0D magnetic topology, despite the large values of some interchain J_{AB} couplings in the real 3D model, sometimes as large as 50 cm^{-1} in magnitude. As a result of the extremely large antiferromagnetic $J(A^T1)$ coupling, the only magnetic state in the range of existence of the LT polymorph which is populated is the ground state, a fact that results in a zero magnetic susceptibility curve over the range of temperatures of the LT polymorph. This trend is identical to that found when the ground state is a closed-shell singlet, which is often described as a 'diamagnetic interaction' as it gives rise to a diamagnetic material. However, all theoretical data we computed on $J(A^T1)$ indicate beyond doubt that the open-shell singlet is the ground state for the A^T1 pair in LT (Table 6), thus discarding the possibility of a closed-shell singlet (i.e., there is no covalent bond formed between the two TTTA molecules). This proves that the large J_{AB} value means that the nearly eclipsed π dimer A^T1 is effectively magnetically silent and that the magnetic topology is in fact zero dimensional.

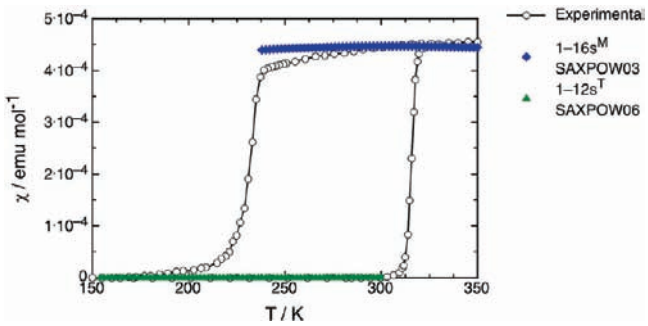

Figure 16. Experimental magnetic susceptibility curve with the two calculated curves for the monoclinic (HT, diamonds) and triclinic (LT, triangles) structures.

The best results we have for calculating the magnetic susceptibility of both phases are shown in Figure 16. The finite magnetic models used are the $1-16s^M$ for the monoclinic (HT) structure and the $1-12s^T$ model for the triclinic (LT) structure. We suspect even better results would be obtained for the monoclinic structure were we to use the $4-16s$ model or a magnetic model of a similar size, but this is currently inaccessible. The results we obtained agree with previous experimentally obtained numbers where curve fitting to empirical models has been used.[3]

Finally, the work done by Awaga et al.[5] to confirm the intrinsic nature of the hysteresis cycle was theoretically investigated. Experimentally, Awaga et al. slowly cooled the HT phase and stopped the cooling on entering the phase transition to the diamagnetic LT phase. Then the sample temperature was gradually raised and the magnetic response monitored. The experimental results of four runs with different starting points, giving rise to 'interrupted' hysteresis loops, are depicted in Figure 17 (empty circles). In every run the plots of $\chi(T)$ clearly indicate that there is little change in the ratio between the HT and LT phases in the temperature range within the loop. Awaga et al. suggested that either very small structural changes modified the magnetic topology (J_{AB}) and in turn the magnetic susceptibility or the two phases could stably coexist in this range. The magnetic topology influence argument was studied by working with a virtual tetraradical structure interpolated between the regularly spaced HT monoclinic and dimerized LT triclinic geometries (see Supporting Information Figure S8). The resulting interpolated magnetic model was a $1-12s^I$ model with alternating $J(A^I1) = -702.91$ and $J(A^I2) = -96.23$ cm^{-1}. The results show that an intermediate structure halfway along the HT $\leftrightarrow$ LT transformation pathway (empty squares in Figure 17a) cannot explain the experimental magnetic response (empty circles). The argument for coexistence of two distinct phases was tested by mathematically mixing the HT and LT magnetic response in different ratios (e.g., the third run depicted in Figure 17b is reproduced by 80% of calculated $\chi(T)$ using HT magnetic data and 20% of $\chi(T)$ using LT magnetic data). Thus, it follows that the magnetic response is correctly reproduced by simply mixing the two phases in this temperature range, in accordance with Awaga's suggestions. The hysteresis is thus intrinsic at least on the time scale of the laboratory.

Conclusions

The geometry and distribution of the magnetic interactions in the monoclinic HT and triclinic LT polymorphs of the TTTA purely organic radical have been studied in detail by performing a First-Principles Bottom-Up study of the available crystals that

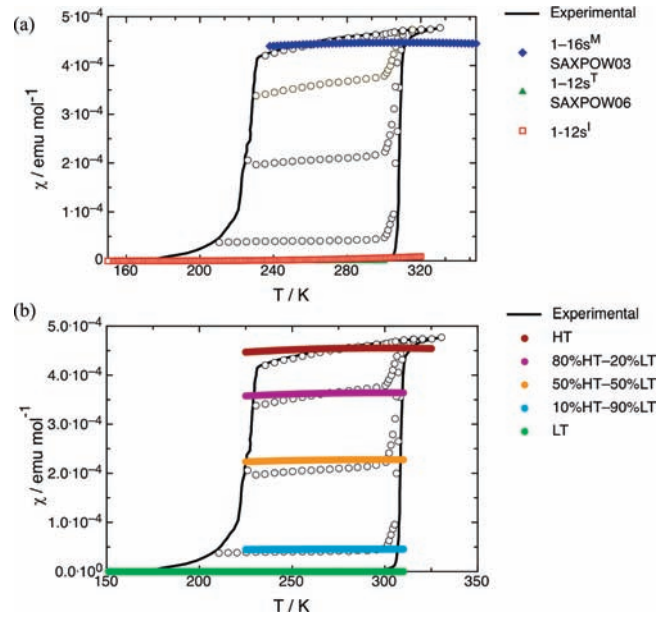

Figure 17. Experimental magnetic susceptibility curve compared to calculated curves using (a) 12 radical chain magnetic model ($1-12s^I$) with J_{AB} values obtained from a virtual tetraradical structure interpolated between the regularly spaced HT monoclinic and the dimerized LT triclinic geometries and (b) a variety of HT and LT mixing, where experimental data is reproduced by 10%HT−90%LT, 50%HT−50%LT, and 80%HT−20%LT. Notice that pure HT monoclinic (dark red) and pure LT triclinic (light green) structures are also shown.

belong to each polymorphic phase. The results obtained indicate that both crystals present a 3D magnetic topology. However, in the monoclinic HT phase, the 3D magnetic topology is dominated by 1D chains ($J_{intrachain} = -135.6$ cm^{-1}, with the largest $J_{interchain} = -10.7$ cm^{-1}, using the room-temperature structure). This fact explains why the energy spectra of a weakly interacting 1D chain model and an isolated chain model are similar, which in turn can be explained and justified using perturbative analysis. Similarly, in the triclinic LT phase, the crystal also presents a 3D magnetic topology but in this case it is dominated by weakly interacting dimers (0D model). Using the room-temperature structure, these dimers present a strong intradimer interaction ($J_{intradimer} = -1755.0$ cm^{-1}), with the largest $J_{interdimer}$ being -50.2 cm^{-1}. These J_{AB} values and the computed magnetic susceptibility curves for the HT and LT phases agree well with previous experimental results obtained by fitting the experimental magnetic susceptibility curve to empirical models (in the HT case, an isolated chain model with a weak mean field term, and in the LT case to an isolated dimer model). DFT/UB3LYP and MRMBMP2 calculations have concurred with the open-shell singlet being indeed the ground state for the radical pair (A1) that dominates the J_{AB} values in the monoclinic HT and triclinic LT crystals. Our analysis supports stable coexistence of the HT and LT phases in the bistability temperature range as postulated previously. Our simulations indicate that a mixing of the magnetic response $\chi(T)$ of HT and LT phases within this temperature range closely describes the interrupted hysteresis loops discussed above, and therefore, hysteresis is intrinsic, at least on the laboratory time scale.

Acknowledgment. We thank the Spanish Science and Innovation Ministry for support (projects CTQ2005-02329/BQU, MAT2008-02032/MAT, and UNBA05-33-001 and Ph.D. grant to J.J.S.), the Catalan DURSI (grants 2005 PEIR 0051/69, 2005-SGR-00036, and

2009-SGR-1203), and the computer time allocated by CESCA and BSC. Furthermore, C.S.C. thanks BSC and the European Community for the award of various grants by HPC-Europa (project RII3-CT-2003-506079 under the FP6 "Structuring the European Research Area" Programme and project 211437 under the FP7 "Coordination and support action" Programme).

Supporting Information Available: Complete ref 25; energies and Cartesian coordinates for monoclinic and triclinic TTTA crystals; interconversion $A^T1 \leftrightarrow A^M1 \leftrightarrow A^T2$; relative geometry of all selected pairs in the monoclinic structure; relative geometry of all selected pairs in the triclinic structure; effect of variation of basis set and data set temperature on computing $\chi(T)$; effect of chain length on computing $\chi(T)$; various magnetic models used to compute $\chi(T)$ in order to account for the three-dimensional nature of the magnetic topology; magnetic susceptibility $\chi(T)$ calculated using magnetic models depicted in Figure S6; geometries for monoclinic HT, triclinic LT, and intermediate structure resulting from interpolating between HT and LT crystal structures. This material is available free of charge via the Internet at http://pubs.acs.org.

JA1057746